AN ABSTRACT OF THE THESIS OF

Sarah Kassem for the degree of Master of Science in Civil Engineering presented on September 5, 2012

Title: Wave Modeling at the Mouth of the Columbia River

Abstract approved:

H. Tuba Özkan-Haller

As the second largest river in the U.S., the entrance to the Columbia River is home to some of the most extreme wave conditions on the Pacific Coast. Winter storms commonly generate waves 6-8 m in height, which in combination with strong tidal currents, can produce dangerous navigation conditions. To improve understanding of the wave dynamics in this complex setting, the SWAN model is applied; 2 hindcasts are conducted and an operations forecast is developed. The model is forced with offshore wave heights obtained from a buoy located in 134 m water depth (for the hindcasts) and a specialized WaveWatchIII forecast (for the forecast). In both cases tidal currents are obtained from SELFE, a circulation model of the Columbia River. The hindcasts are validated through measurements obtained from an inshore buoy located in 25 m water depth, a 4-week field experiment and remote sensing methods. The model performs best at the location of the buoy, with a normalized root-mean-squared error (NRMSE) of 11%, primarily because it is outside the area of strong tidal currents. Within the river mouth, the model is able to predict the changes in the wave field due to currents, but its performance is limited by errors in velocity estimates and strong shears in the tidal current profile. From the modeling work, it is evident that wave transformations at the mouth of the river are dominated by the tidal currents. The forecast has been operational since August 2011 and provides 45-hours of predictive wave information. In comparison with measured wave heights at the buoy, the forecast performs well, with a NRMSE of 16%. The majority of errors are caused by errors in the input conditions, since they themselves are forecasted. Additional errors arise from phase-resolved properties in the wave field that the model is unable to produce; these errors are also present in the hindcasts.

Despite the limitations, this forecast provides valuable information to bar pilots since it includes the effects of the tidal currents.

Wave Modeling at the Mouth of the Columbia River

by

Sarah Kassem

A THESIS

submitted to

Oregon State University

in partial fulfillment of
the requirements for the
degree of

Master of Science

Presented September 5, 2012

Commencement June 2013

Master of Science thesis of Sarah Kassem presented on September 5, 2012

APPROVED:

Major Professor, representing Civil Engineering

Head of the School of Civil and Construction Engineering

Dean of the Graduate School

I understand that my thesis will become part of the permanent collection of Oregon State University libraries. My signature below authorizes release of my thesis to any reader upon request.

Sarah Kassem, Author

ACKNOWLEDGMENTS

Several people contributed to the successful completion of this thesis; first and foremost is my adviser, Tuba Özkan-Haller. She has been an amazing adviser and teacher and somehow always manages to find a way to explain the most complicated processes in the simplest of ways. Data for this project came from a number of sources; David Honegger was a substantial help with the marine radar data and all the questions I had about it and big thanks to the people from OHSU-CMOP for allowing us use of the tidal current data. A monumental amount of gratitude must be given to everyone in the CIL Lab who always had the time for my many, many question. I would also like to thanks Peter Ruggiero, Dave Hill and Kendra Sharp for serving on my committee.

Friends! They are truly the best things in the world, they made my two years here unforgettable. Shred Fierce.

TABLE OF CONTENTS

LIST OF FIGURES

LIST OF TABLES

Wave Modeling at the Mouth of the Columbia River

1 Introduction

The Columbia River is the largest river on the Pacific coast of the U.S. and the second largest river in the U.S.; the estuary is a heavily engineered waterway with large jetties that mark the entrance and an annual dredging program to maintain the navigational channel. The maintenance of the estuary is essential to the local and state economy. Several ports are located along the river and it transports $14 billion worth of goods to international markets every year (Moritz et al. 2007). Known as the "graveyard of the Pacific", the Columbia River is notorious for its extreme winter wave heights and large tidal currents (Haglund, 2011). Large waves propagating across the Pacific Ocean collide with strong currents and variable bathymetry at the mouth of the river to produce adverse conditions for navigation. An understanding of the key hydrodynamic processes at the mouth of the Columbia River (MCR) is needed to determine the response of waves to future bathymetric changes (from dredging and natural morphological evolution) and to provide insight into navigation safety. Forecasts of wave conditions are especially advantageous because it gives navigators and bar pilots an estimation of future wave conditions, thus allowing for a safer and more efficient passage into the river.

Using numerical models to quantify wave transformations is an effective way of determining the important hydrodynamic processes as it allows users to exclude certain physics in order to focus on significant processes. SWAN (Simulating WAves Nearshore), a phase-averaged spectral wave propagation model, is a well established model that has been tested in coastal environments on many occasions (Booij et al., 1999; Moghimi et al., 2005; Gorrell et al., 2011). Rogers et al. (2007) used SWAN to forecast waves in the southern California Bight and tested the sensitivity of their forecasting system to computational resolution, stationarity assumptions and boundary forcings. Wave-current modeling requires information on estuarine currents, either in a one-way interaction, where currents affect the waves, or a 2-way interaction, where the effect of the waves on the current is also taken into account. The latter method was recently employed by Olabarrieta et al. (2011), who used a SWAN-ROMS coupled model to investigate the wave-current interaction at Willapa Bay with successful results.

There has been much interest in wave transformations at the MCR over the past 30 years. González (1984) used a 10-day buoy deployment to identify the important wave transformation processes near the entrance. He found large wave amplification due to ebb currents and moderate attenuation due to flood currents. He was able to model the wave height transformation at the MCR with surprising accuracy under the assumption of straight and parallel depth contours. González et al. (1985) used radar imagery to observe large current refraction at the entrance to the jetties. Several reports have been published by the United States Army Corps of Engineers (USACE) documenting the transformation and amplification of waves at the MCR. These studies used a 2DH spectral wave model to analyze the waves, not accounting for the effect of tidal currents (USACE, 2003, 2008). Furthermore, Michalsen et al. (2006) employed a phase-resolving Boussinesq model at the river mouth to determine the wave response to dredging and a potential borrow pit. In the absence of currents, they found refraction at the river mouth to be the governing wave transformation, as waves turn to become aligned with the jetty and the contours of the river. Recently, coupled models have been adopted at the MCR to capture the interaction between the currents and waves; these studies focused on wave transformation due to currents only, mainly concentrating on locations in the channel. van der Westhuysen and Elias (2010) applied Delft3D to MCR to validate SWAN's improved whitecapping formulation. Using a similar model setup and focusing on sediment transport and process based modeling, Elias et al. (2012) were able to capture the significant features in the wave and current fields at the river mouth.

This study aims to further understand the wave transformation processes due to both bathymetric and current effects at the MCR, using a one-way wave-current coupling scheme. Two hindcasts are conducted; the first hindcast models a 4-week field experiment in August and September 2005, at the mouth of the river, and is used to validate the wave-current interaction modeling at the river mouth (Moritz et al., 2005). The second hindcast occurs in March 2010 and the results are compared against a surface buoy and data from a marine radar. In addition, an operational forecast is developed which provides predictions of wave conditions, including the effects of the tidal current, for the purpose of navigation safety.

2 The MCR environment

The entrance to the Columbia River is marked by jetties, the north arm extending 0.8 km offshore, the south arm, 4 km offshore and Jetty 'A', protruding south from the northern bank of the river (see Fig. 1b). Prior to construction, the entrance to the river was continually migrating in order to maintain a balance with the hydrodynamical forcings of the ocean and river. Between 1885 and 1917, jetties were constructed on each flank of the river, stabilizing the entrance and initiating large morphological change (Kaminsky et al., 2010). The installation of the jetties brought a large pulse of sediment (300-600 Mm^3) to Peacock Spit and Clatsop Spit, the north and south tidal shoals, respectively. Over the last century there has been a continuous receding of these shoals as sediment is spread out to the nearby beaches as the morphology gradually responds to the hydrodynamics. The magnitude of bathymetric change rates at the MCR have decreased since the completion of the jetties, indicating that the area is coming to a new state of equilibrium; however the relatively slow change in these rates indicate that full equilibrium will take several more decades to reach (Kaminsky et al., 2010; Ruggiero et al., 2005). In addition to the natural tidal shoals, artificial shoals have been created through the disposal of dredged sediment which significantly alter the wave transformations. The annual dredging program maintains a 905 m wide and 17 m deep navigational channel. This results in an average of 4.5 million cubic yards of dredged sediment every year, 75% of which is currently placed at 2 sites within the nearshore region of the MCR. One of these sites is located off the tip the north jetty and the sediment placed there is intended to prevent further erosion to Peacock Spit (Moritz et al., 2007).

As the shoals that once protected the jetties erode, the jetties have become more exposed to the violent wave conditions, and their integrity is threatened (Moritz et al. 2007; Mortiz et al. 2003). In a 2003 report, the USACE stated that the majority of wave amplification near the north jetty is due to wave focusing on Peacock spit, and over the last decade, the quick recession of the spit has allowed for larger waves to break closer to the jetty and channel (USACE, 2003). The MCR is also home to its infamous "bar", an approximately 10 km^2 ebb tidal delta, located 4 km from the jetties.

The U.S. Pacific coast is known for its severe wave climate; strong winds blowing over the Pacific Ocean create large waves and long period swell (Tillotson and Komar, 1997). Winter storms come from the southwest, bringing average winter waves of 3

meters with a period of 12-13 seconds, however, extreme wave heights of 14-15 m have been observed (Allan and Komar, 2002; Ruggiero et al., 2005). Summer conditions are smaller, with an average wave height of 1.2 meters and period of 8 seconds. Waves generally come from the northwest and there is an approximately 30 cm decrease in monthly mean water levels compared to the winter months. Tidal conditions are semi-diurnal, with a 2 to 4 meter range and tidal velocities at the MCR range from over 2 m/s on ebb to 1 m/s on flood tide (González, 1984; Ruggiero et al., 2005; Horner-Devine, 2009).

The Columbia river drainage basin is 660,500 km^2, stretching from southern British Columbia and Alberta to Montana, Idaho and Oregon. The main arms of the river converge 150 km upstream of the entrance to give a mean annual flow in the river of 6,000 m^3/s. The estuary is characterized by energetic flows, large salinity gradients and temporal variability which are all caused by the strong tidal currents and large river flow (Simenstad et al., 1990). The river is a significant source of freshwater input for the area between San Francisco Bay and the Straight of Juan the Fuca (Simenstad et al., 1990). The plume created by the fresh water outflow, which extends beyond the continental shelf, tends to follow one of two basic structures depending on the season; during the fall and winter the plume will be oriented towards the northwest and in the spring and summer it tends to the southwest. However, the direction, thickness and width of the plume is highly dependent on the wind strength and direction (Hickey et al. 1998). Coriolis forces and a shallow coastal region north of the mouth tend to make the plume move north; however, this is made more difficult by the angle of the jetties, which are pointing southwest. Local winds will either reinforce or counter this behavior (Baptista et al. 2005). The Columbia estuary is subject to extreme variations in stratification and salinity intrusion, and because of this, experiences strong vertical shears in velocity (Hamilton, 1990). Due to the relative narrow entrance, the MCR has a larger volume flux at the estuary than comparable river systems (Hickey et al. 1998).

Two buoys are located close to the MCR. The first is National Data Buoy Center (NDBC) buoy #46029, a buoy located in 134 m water depth, on the continental shelf. The second buoy is a Coastal Data Information Program (CDIP) buoy, located 5 km southwest of the south jetty, in 25 m water depth, relative to NAVD 88. This buoy is used to validate the inshore wave parameters obtained from the model. There is a small tidal signature in the wave heights at the CDIP buoy, and at times during strong flows, it has been known to be pulled under water (Dan Jordan, personal

conversation). Limited data are available for the area within the entrance to the river; strong shears in the current and large wave heights make instrument deployment and survivability difficult.

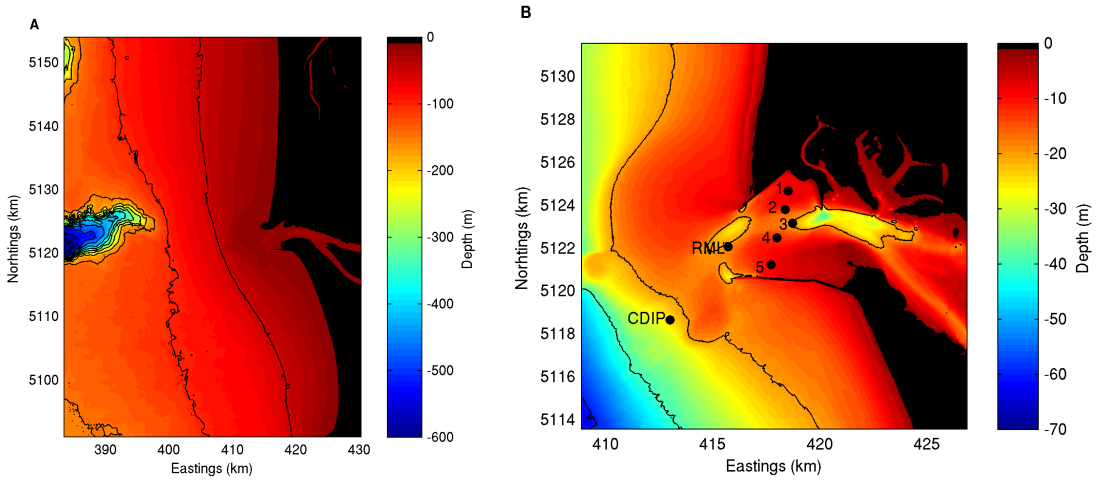

Figure 1: A. Bathymetry of model domain with contour lines in 50 m increments, starting at 600 m depths. B. Model domain zoomed in to show the variable bathymetry of river mouth. Points 1 to 5 are station locations during the Mega Transect Experiment. Stations 1 to 3 measured water levels and currents with an ADP and station 4 and 5 measured waves, water levels and currents with an ADCP and ADV. Also shown is the CDIP buoy and the river mouth location (RML), which is an arbitrary output location in the model. Contour lines are located at 60 m, 40 m, 20 m and 0 m water depths.

3 Methodology

To understand the dominant wave transformations at the MCR, two hindcast simulations are conducted using SWAN and an estuarine circulation model. The first hindcast models the time period from August 8 to September 8, 2005. During this period, a field experiment was conducted at the entrance to the MCR in which wave and tidal current information was recorded across the river mouth (Moritz et al., 2005). This hindcast is conducted to compare model results at the river mouth with measured data from the field experiment. A second hindcast is conducted for the entire month of March, 2010; this period was chosen because it overlaps with a 2-day radar deployment at the base of the south jetty. Finally, an operational forecast of the Columbia River is developed which provides short-term wave predictions at the MCR.

3.1 Physics

In the presence of a current, wavelength is governed by the dispersion relation which, for linear wave theory, states that:

$$\sigma = \omega - kU = \sqrt{gk \tanh kh} \tag{1}$$

where σ is the relative angular frequency (i.e. moving with the current, U), ω is the absolute angular frequency, k is the wavenumber, and h is the water depth. In a steady opposing current (where $U < 0$), k increases, and for a following current, k decreases. ω is constant, regardless of the current. From eq. 1, we can differentiate with respect to k to obtain the effect of the current on the group velocity, C_g:

$$\frac{\partial \sigma}{\partial k} = \frac{\partial \omega}{\partial k} - \frac{\partial}{\partial k} kU$$

$$C_{gr} = C_{ga} - U$$

where C_{gr} is the relative group speed and C_{ga} the absolute group speed. This shows that in a following current, C_{ga} will increase and for an opposing current, C_{ga} will decrease. In the extreme case, if the relative group speed is decreased to the point of being equal and opposite to the current, the wave will be blocked by the current.

The wave action, N, defined as $N = \frac{E}{\sigma}$, where E is the wave energy ($E = \frac{1}{8}\rho g H^2$), is conserved in the presence of a current. In a following current, σ decreases; to

maintain conservation, E will decrease as well, which will result in a decrease in wave height, H. The same is true for an opposing current; σ increases, leading to an increase in E and therefore H. In general, and as noted in Peregrine (1976) and Jonsson (1990), following currents will create longer waves with lower wave heights and opposing currents will steepen the waves, giving shorter wavelengths and higher wave heights.

Currents also focus and defocus wave energy via refraction. Snell's law, ($\frac{\sin\alpha}{C} = const$), which governs the process of wave refraction over straight and parallel contours, states that waves will change direction (α) when the wave speed (C) is altered. In an opposing current, speed is reduced and thus, to maintain Snell's constant, $\sin\alpha$ will also reduce, so α will become more shore normal. In the case of a following current, the opposite effect is seen, and waves will become more shore parallel. This theory assumes a homogenous and steady current field and locally plane waves. The time rate of change of the currents is usually small with respect to the time scale of the waves, so the first assumption is met, however, in a complex 2D domain, such as the MCR, waves are not necessarily locally plane. This means that in an opposing current, waves will not necessarily orient themselves shore normal, instead, they will turn to head towards the region of strongest current. In a following current, waves will turn to head away from the region of strongest current.

3.2 The SWAN Model

The SWAN model is a 2 dimensional depth-averaged phase averaged 3rd generation spectral wave model governed by the conservation of wave action. As waves propagate through the domain, the wave action is modified through shoaling and refraction, and SWAN accounts for changes in both spatial and spectral domains. For the simulations discussed in this study, options for additional wind growth, bottom friction, and non-linear considerations are turned off and all the simulations are conducted in steady state. The dissipation of wave action occurs through depth-induced breaking, based on the Battjes and Janssen (1978) breaking dissipation model, and the whitecapping formulation, given by Komen et al. (1984).

In the presence of an opposing current, the Komen et al. (1984) formulation allows for a wave steepness greater than observed, thus underpredicting dissipation due to opposing currents (Ris and Holthuijsen, 1996). It calculates dissipation based on mean spectral steepness, causing an overprediction of energy in the spectral tail (Rogers

et al., 2003). van der Westhuysen et al. (2007) proposed a saturation-based whitecapping formulation which was found to give less energy in the spectral tail, resulting in more accurate predictions of wave periods. This new method is not affected by background swell because it treats dissipation as a function of local frequency. van der Westhuysen and Elias (2010) used SWAN used to model the wave-current interaction at the MCR. For this, they tested the enhanced whitecapping formulation given by van der Westhuysen et al. (2007) and found it to give more accurate results than the Komen et al. (1984) whitecapping scheme.

3.3 The SELFE Model

The tidal elevation and current information is obtained from SELFE, a large-scale 3D baroclinic circulation model specifically designed for the Columbia River estuary (Zhang et al., 2004). It solves the shallow water equations using the Boussinesq approximations, mass conservation and conservations of salt and heat to give water surface elevation, 3D velocity fields, salinity and temperature throughout the domain (Zhang et al., 2004). The SELFE model domain runs from southern British Columbia to California and extends offshore to the continental shelf; inland it extends 240 km up the Columbia river to the Bonneville Dam and Willamette falls. Included in the model are the Strait of Juan de Fuca, the Georgia Strait and Puget Sound. River inputs come from the Bonneville Dam for the main branch of the river and Newberg, OR for the Willamette River. Model forcings also include the Fraser river watersheds, 4 diurnal and 4 semi-diurnal tidal constituents, ocean salinity and temperature and atmospheric forcings, given as atmospheric pressures, air temperature and specific humidity (Baptista et al., 2005). It is a finite element model with variable resolution, but at the river mouth, resolution ranges from 200 m to 500 m. The results of the SELFE model are provided by the Center of Coastal Margin Observation and Prediction (CMOP). Although SELFE is a 3D model, the tidal velocities are depth averaged in order to be incorporated into SWAN, which can only account for depth uniform currents.

3.4 Hindcasts

The hindcasts are modeled using SWAN on a domain 63 km in the alongshore and 47 km in the cross-shore (see Fig. 1a). The bathymetry is composed of Digital Elevation Model (DEM) data from 2003 by the National Geophysical Data Center (NGDC)

for the Astoria, OR domain. A 2005 bathymetry survey of the rectangular area 15 km north-south by 10 km east-west centered about the jetties by the USACE is incorporated into the DEM data. For the March 2010 hindcast, nearshore bathymetry data from July 2010 are also included. The bathymetry data are interpolated to a regular grid with 30 m spacing. The computational domain is nested once to obtain a finer resolution at the river mouth; the coarse grid has a resolution of 75 m in the cross-shore and 100 m in the longshore, and the fine grid, which begins 26 km from the offshore boundary and extend north-south for the length of the domain, has resolution of 30 m x 50m (cross-shore x longshore). Inputs incorporated into the model are the offshore wave conditions, the tidal currents and the water surface elevations. Wave conditions are obtained from NDBC buoy #46029, which is located on the offshore boundary of the model domain and provides full directional spectra in hourly increments. The lateral boundary conditions are determined by shoaling the offshore spectra along straight and parallel contours obtained from the northern most and southern most bathymetry cross-shore sections.

3.5 Forecast

The forecast domain is composed of the 2003 DEM data and the 2005 USACE data. The model is not nested, resulting in a computational resolution of 100 m in the longshore and 75 m in the cross-shore. Results from the hindcasts, though, show that there is insignificant change in model results between these two levels of resolution. Forecasted wave information is obtained from NearWaveWatchIII, a forecast that is developed specifically for the Pacific Northwest (PNW) (García-Medina et al., 2012). It has a nearshore resolution of 30 arc-seconds, which is finer than the standard WaveWatchIII model with a resolution of 15 arc-minutes. This more refined forecast (referred to as NearWW3) is able to capture the effects of variable offshore bathymetry (García-Medina et al., 2012). The domain of this forecast extends from approximately central Washington to northern California. The NearWW3 forecast is produced daily, giving 84 hour predictions of wave information in hourly increments. Spectral information is extracted from the NearWW3 forecast at the boundary of the MCR model domain at approximately 1 km increments. Forecasted tidal current information is obtained from the SELFE model which runs daily, producing 72-hour of data, providing the tidal current velocity field and water surface elevation on an hourly basis. The NearWW3 forecast is completed at 18:00 of day 1 and the SELFE

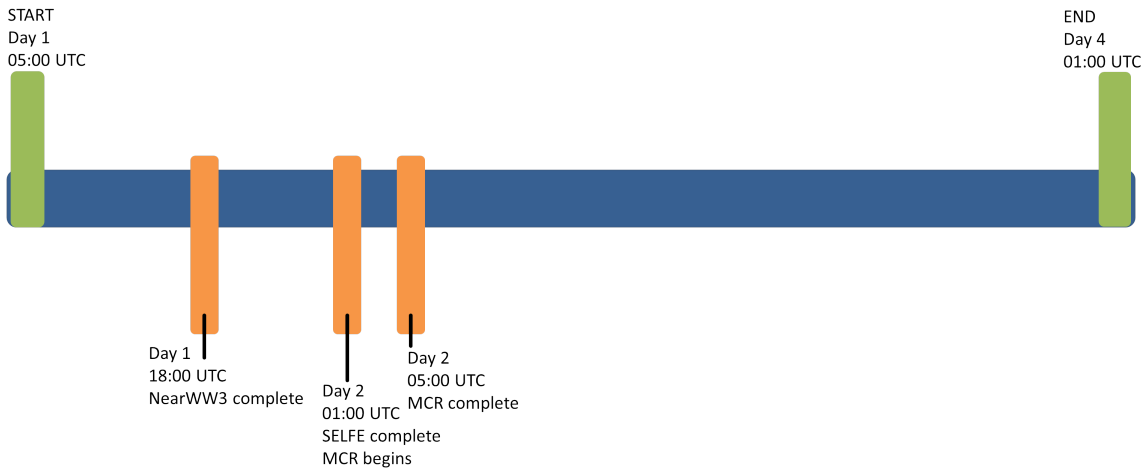

Figure 2: Timeline of MCR forecast. Total forecast length is 69-hours, with 45 hours of true forecasted data.

forecast is completed by 01:00 on day 2; the MCR forecast thus starts everyday at 01:00, and takes 4 hours to complete, giving results from 05:00 day 1 to 01:00 day 4. The total forecast length is 69-hours, with 45 hours of true forecasted information (see Fig. 2).

4 Results

4.1 August 2005 Hindcast

In August and September 2005, The Mega Transect Experiment (MGT) was conducted by the USACE in collaboration with the United State Geological Survey (USGS) with the aim of quantifying the sediment transport through the river mouth. Instruments were mounted on tripods 2-3 m in height and deployed at five locations across the river (see Fig. 1b). Upward looking acoustic doppler current profilers (ADCPs) measured the waves, current profiles and water levels and near bottom orbital velocity measurements were made with acoustic doppler velocimeters (ADVs) (Elias and Gelfenbaum 2009). The offshore wave conditions for the duration of the experiment were small, with a mean wave height of 1.3 m and peak period of 8.2 s, but within the normal range for this time of year. Wave direction[1] is generally from the west and north-west, except for the few days between Aug 20-21 and Sept. 6-7 when waves are coming obliquely from the southwest (see Fig. 3). This experiment provides an opportunity to validate not only the modeled wave heights, but also the tidal currents obtained from SELFE. The results from the model will be compared against results from station 4, since it is the most representative of wave conditions in the center of the channel.

In order to obtain accurate model results at the river entrance, where wave-current interactions are expected to be prominent, the velocity field must be well represented. The SELFE model does a very good job of predicting the along-channel currents with a normalized root-mean-squared error (NRMSE) of 12%. Occasional differences in the model and data occur, mainly on ebb tides, when the model has a tendency to overpredict. The model consistently underpredicts the cross-channel currents, especially on southward directed flows, resulting in a NRMSE of 19%. Cross-channel current magnitude is approximately half of the along-channel current magnitude, so errors in the cross-channel velocities are not as significant. However, this underprediction of cross-channel currents creates a current that is more wave parallel than the observed currents, which would induce a larger effect on the waves.

There is a clear tidal signature in the wave heights at station 4, where wave heights increase on ebb tides and decrease on flood tides (see Fig. 4). The pattern is well represented by the model, however it does not capture the maximum and minimum

[1] Wave direction is specified in Cartesian coordinates; counterclockwise from due west, indicating the direction the wave is going to.

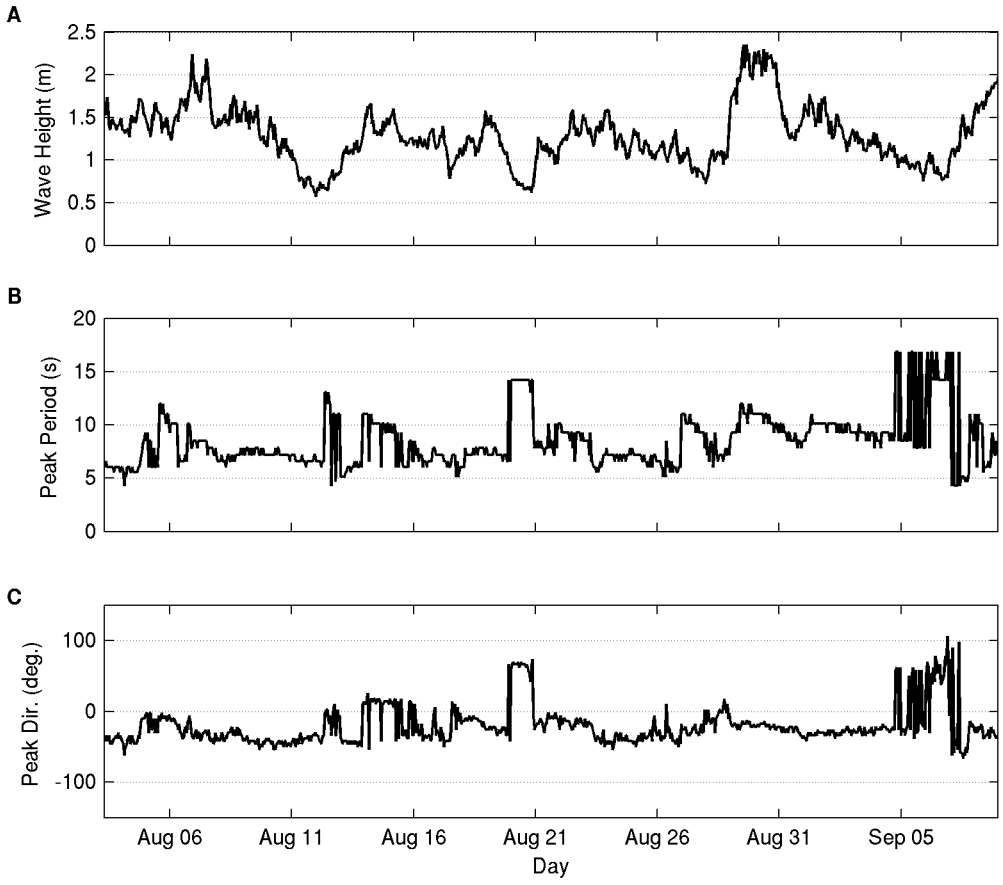

Figure 3: Offshore wave height, peak period and peak direction obtained from NDBC buoy 46029 for the duration the MGT experiment.

Table 1: Results for the August 2005 hindcast at station 4. RMSE is the root-mean-squared-error, NRMSE is the normalized root-mean-squared-error.

	H_s stn. 4	T_p stn.4	T_m stn. 4
RMSE	28 cm	3.0 s	0.9 s
NRMSE	30 %	39 %	12 %
BIAS	11 cm	0.4 s	0 s
REL. BIAS	11 %	5 %	0 %

extent of change. It typically overpredicts the wave height increase due to the ebb current and underpredicts the decrease in wave height due to flood currents. At station 4, the model has a NRMSE of 30%; Table 1 gives the model statistics of this hindcast period. Mean period is better represented than peak period because there were many instances of dual peak spectra in which the model did not correctly predict the peak frequency. The modeled wave heights are overpredicted, with a relative bias of 11 %, suggesting that an insufficient amount of energy is being dissipated between the offshore boundary and the river mouth. The two sources of dissipation in the model are depth-induced breaking and whitecapping. Bottom friction is not activated as this has been shown to be negligible on small domain such as this one, however including it could potentially cause a minor improvement in bias (García-Medina et al., 2012). Depth-induced breaking occurs over the tidal shoals and at times in the channel during large wave events, however waves during the experiment were small and thus, breaking was not significant (Elias et al., 2012). Additional errors can arise by not accounting for the effect of the waves on the currents. This would be most significant over the shoals where waves break, producing wave-induced currents. The effect of this interaction would fluctuate depending on the tidal cycle and would be most pronounced during large wave conditions, when wave-induced currents are significant. In strong ebb currents, steepness limited breaking, or whitecapping, does occur. The entire simulation was run again using the saturation based whitecapping formulation proposed by van der Westhuysen et al. (2007). Minor differences in wave heights between these two cases occur; the van der Westhuysen et al. (2007) method consistently reduces wave heights on ebb currents which results in a NRMSE of 29% and a bias of 10 %, which are improvements, albeit minor.

Measured currents in the MCR are heavily sheared with vertical vorticity ranging from 0.2 s^{-1} to -0.1 s^{-1} in the along-channel direction and 0.05 s^{-1} to -0.05 s^{-1} in the cross-channel direction. Over the 10 m water column, a vertical vorticity of

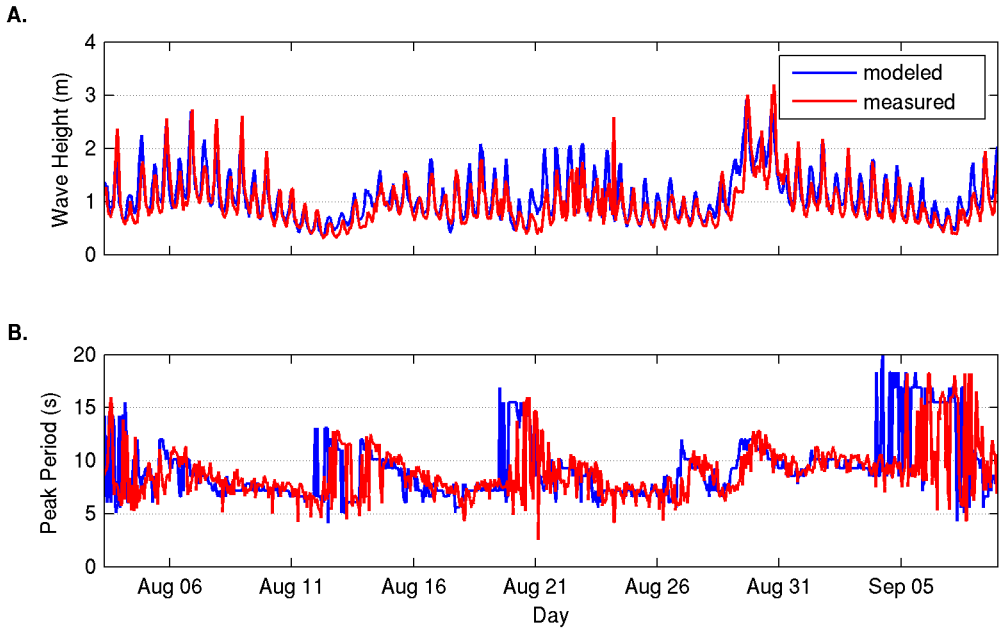

Figure 4: A. Modeled and measured wave heights at station 4 during the MGT experiment. B. Modeled and measured peak periods at station 4.

0.2 s^{-1} translates to a velocity difference of 2 m/s. Shorter period waves will only be affected by the top portion of the current profile, which can create errors when depth-averaged currents are used. Generally, currents in the top half of the water column have a greater magnitude. Currents which are depth averaged over the top half of the water column have a velocity that is approximately 20% to 30% greater than currents averaged of the entire water column. Thus, in the model, higher frequency waves are exposed to a weaker current, resulting in a reduced effect on the waves. In their modeling efforts at the MCR during the MGT experiment, Elias et al. (2012) used a modified current averaging method of Kirby and Chen (1989) in which the currents were weighted by mean wave number. This method gave the best model results and is, physically, the most realistic method of averaging the vertical current profile. The Elias et al. (2012) study used the fully coupled Delft3D model and accounted for additional physics such as wind-wave generation, bottom friction, and non-linear interactions. The results from that study compare well against those obtained from the August hindcast. Errors in the wave height and mean period at station 4 are very close and the model skill in the tidal currents estimates fall within a few skill points of each other.

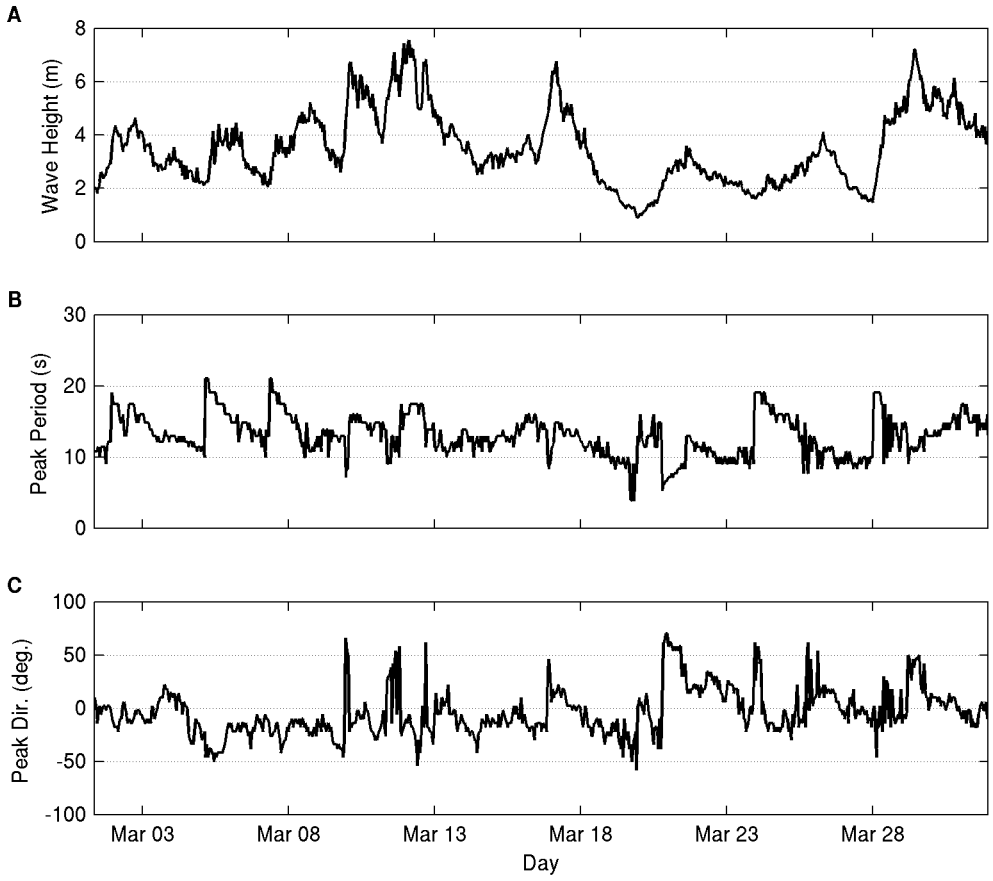

Figure 5: Offshore wave height, peak period and peak direction obtained from NDBC buoy 46029 during the March 2010 hindcast.

4.2 March 2010 Hindcasts

The average offshore wave condition during the March 2010 hindcast period was a significant wave height of 3.5 m, peak period of 13 s and peak wave direction of -3º. Several large storms occurred during this time, with 4 storms generating waves 6 m or higher (see Fig. 5). Two sources of validation are available for this period; the CDIP buoy, installed in 2009, which gives directional and spectral wave information on an hourly basis, and a marine radar, which was stationed at the base of the south jetty for a 24 hour period at the end of the month.

Table 2: Results for the March 2010 hindcast at the CDIP buoy. RMSE is the root-mean-squared-error, NRMSE is the normalized root-mean-squared-error.

	H_s buoy	T_p buoy	T_m buoy	D_p buoy	D_m buoy
RMSE	34 cm	1.9 s	1.2 s	12^{o}	9^{o}
NRMSE	11 %	16 %	16 %	-	-
BIAS	-9 cm	-0.2	0.8 s	-2^{o}	2^{o}
REL. BIAS	-3 %	-1.4 %	9 %	-	-

4.2.1 Comparison with the CDIP buoy

The model does well at predicting wave heights at the CDIP buoy, with a NRMSE of 11% and a relative bias of -3% (see Fig. 6). Peak period and direction are also well predicted, but with less accuracy than the wave heights; refer to Table 2 for a summary of model results. The latter half of the time series shows a high fluctuation in the measured period, which is evident of a dual peak spectra. Errors in modeling the peak period during these situations are not representative of model skill, since small errors in the relative magnitudes of multiple peaks can lead to misidentification of the true peak, resulting in a large numerical difference in wave period. The peak wave direction at the buoy is, except for a handful of cases, consistently from the south. Offshore, however, waves are coming from either the north or south, suggesting that the bathymetry near the buoy causes the waves to approach from the south, regardless of the offshore direction. This is seen in Fig. 7, where waves initially coming from the northwest will refract to approach from the southwest at the buoy, but waves originating from the southwest tend to remain from that direction.

4.2.2 Comparison with the marine radar

Large wave refraction occurs at the MCR; evidence of this has already been seen at the CDIP buoy. Near the river mouth, point comparisons through buoys or other in-situ instrumentation do not provide data with a large enough spatial density to resolve the sharp refractions that are expected at the entrance. The use of remote sensing through marine radar observations provides an opportunity to validate wave directions over a portion of the domain. On March 30, 2010, a marine radar was stationed at the base of the south jetty. The radar collected 21 hours of data; in each hour, the antenna rotated 512 times. The first half of collection had a mean rotation per minute (RPM) of 36, resulting in a collection time of 14 to 15 min and

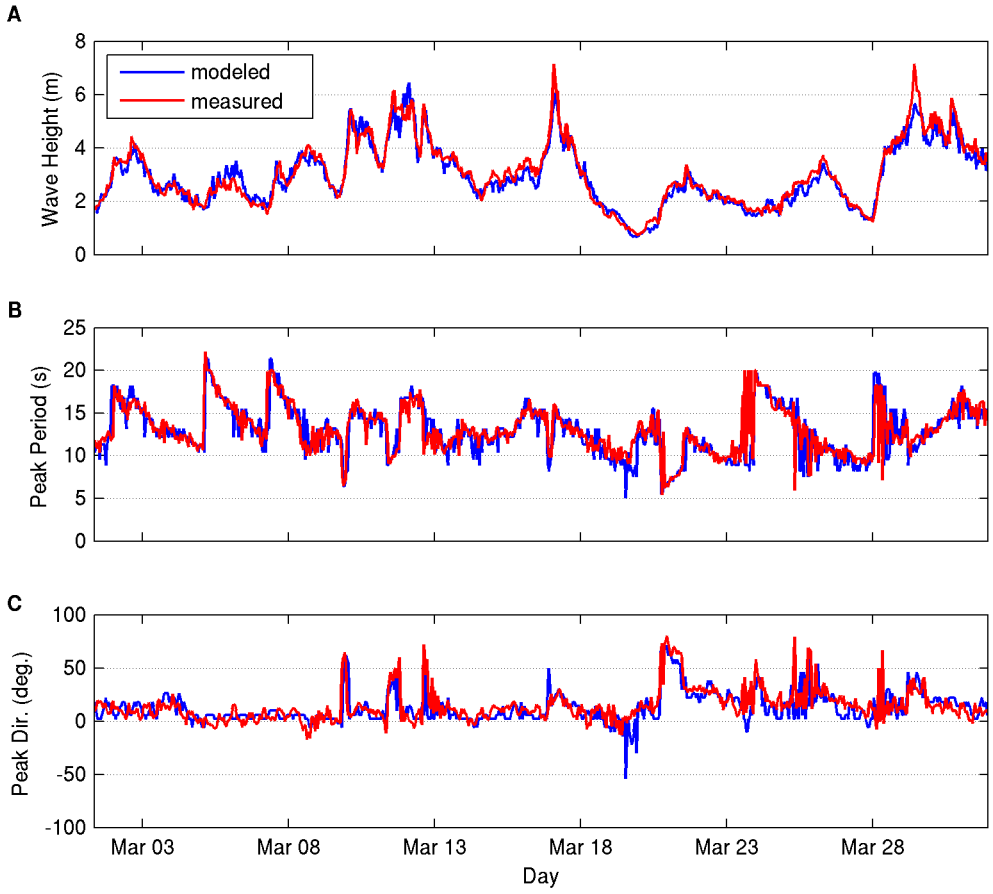

Figure 6: Modeled and measured wave heights (A), peak periods (B) and peak direction (C) at the CDIP buoy during the March 2010 hindcast.

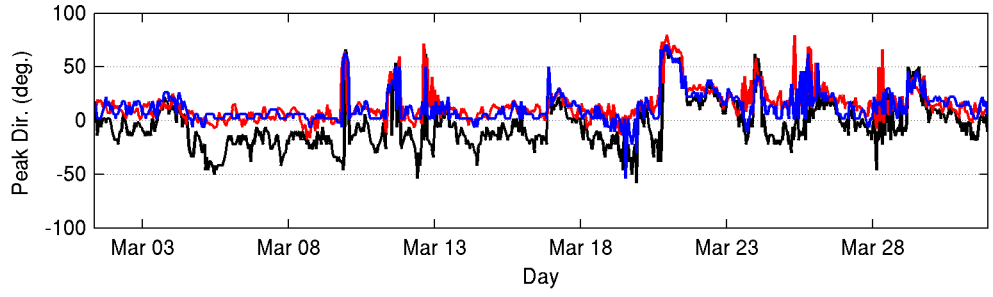

Figure 7: Modeled (blue) and measured (red) peak direction at the CDIP buoy during March 2010. Offshore peak direction is shown in black.

the second half had a RPM of 48, with a collection time of 11 to 12 min. Using cross-spectral correlation, wave directions are extracted for each hour of radar collection (Plant et al., 2008). Comparisons are made by isolating one SWAN simulation and the corresponding radar data from that hour for both an ebb and flood tide case (see Fig. 8 and 9). In both cases, the offshore wave direction is from the southwest; south of the jetty, waves refract to a more oblique southwest direction (positive angles in Fig. 8 and 9), as they align with the south tidal shoal. Negative angles (waves from the north) are seen to the north of the jetty, as waves refract around the jetty and align themselves with the bathymetry of the river mouth. Quantitative comparisons are shown in Fig. 10 and 11, which shows modeled and measured wave directions for 2 cross-sections in the radar footprint (black lines in Fig. 8). Radar observations can be noisy and thus, a 7-point moving average of the measured wave direction is also plotted. In the east cross-section, a sharp change in direction over a short distance is seen in the modeled wave direction, where waves are shifted obliquely to face the south before gradually returning to face the west. This refraction pattern is likely due to bathymetric effects since it occurs in both tidal cases. The RMS errors for the flood case are 13^{o} and 17^{o} for the left and right cross-section, respectively, and for the ebb case are 16^{o} and 23^{o} for the left and right cross-section, respectively.

4.3 Forecast

The forecast has been operational since August 2011, providing wave height and directional information at every point in the computational domain, and spectral information at the CDIP buoy. The results of the first 24 hours of every forecast are linked together to form a continuous time series of wave parameters. This is shown for the 6 month period of August to December 2011 in Fig. 12. At the CDIP buoy, the forecast has a RMSE of 38 cm and a NRMSE of 16%. The performance statistics for this time period at the CDIP buoy are given in Table 3. The majority of the errors are derived from the input waves since they are also forecasted, as is seen in Fig. 13, which correlates the ratio of modeled and measured wave heights. The NearWW3 forecast has a minor tendency to overpredict wave heights with a 4% positive bias. However, as waves propagate from the offshore boundary to the buoy, the bias is overcompensated by the model, resulting in a bias of -3% at the buoy. Rogers et al. (2007) emphasized the importance of accuracy in input conditions in hindcasting and forecasting models, as there is the potential of errors in the input conditions being

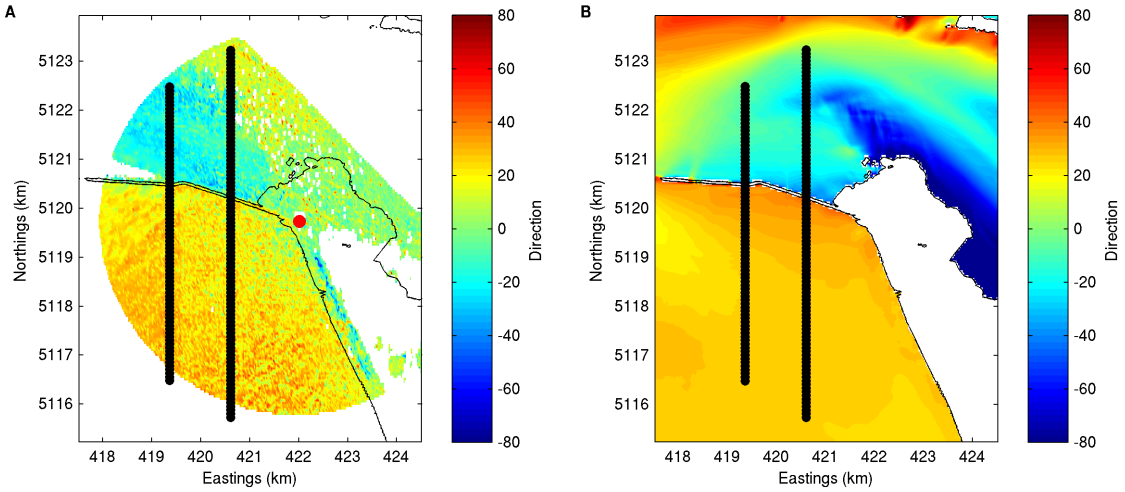

Figure 8: Measured (A) and modeled (B) mean wave directions for March 30 00:00. Mean offshore direction for this time is 23^{o} and the along-channel current is 1.1 m/s. The black lines are the location of the cross-shore transects shown in Fig 10. The red point in Fig. A is the location of the radar; data north and east of this point is unreliable since the radar reflects of off the land.

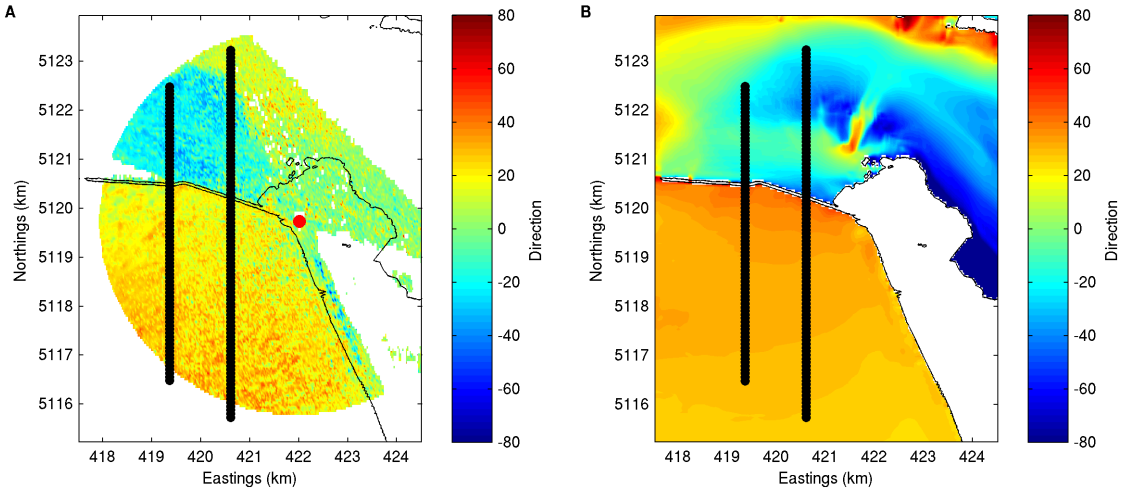

Figure 9: Measured (A) and modeled (B) mean wave directions for March 30 03:00. Mean offshore direction for this time is 17^{o} and the current in the channel is -2 m/s. The black lines are the location of the cross-shore transects shown in Fig. 11. The red point in Fig. A is the location of the radar; data north and east of this point is unreliable since the radar reflects of off the land.

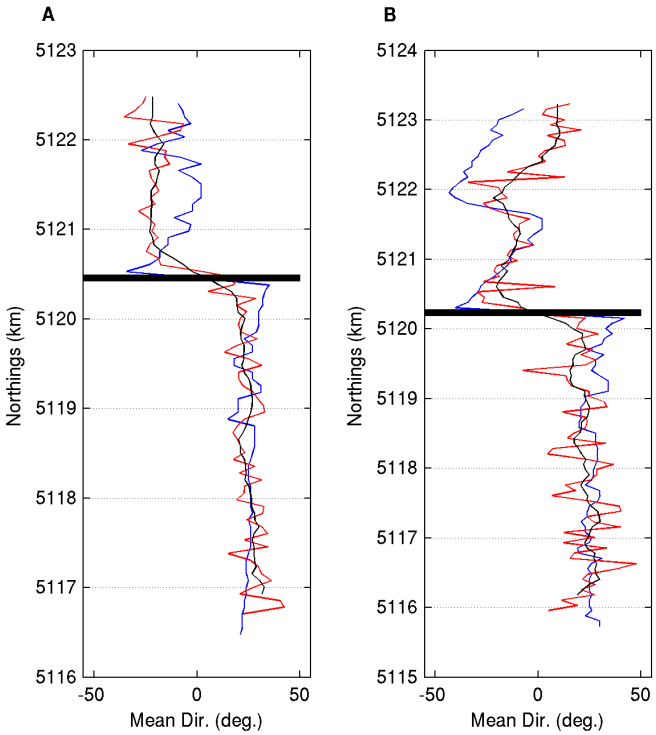

Figure 10: Modeled (blue) and measured (red) mean wave directions for 2 cross-sections located in the radar footprint for March 30 00:00. Offshore mean wave direction is 23^{o} and velocity in the mouth is 1.1 m/s The black line is a 7-point moving average of the measured wave direction. The modeled values are obtained by averaging the direction over the top 4 coherent frequencies obtained from the cross-spectral correlation analysis. Fig. A refers to the west section and Fig. B refers to the east section in Fig. 8.

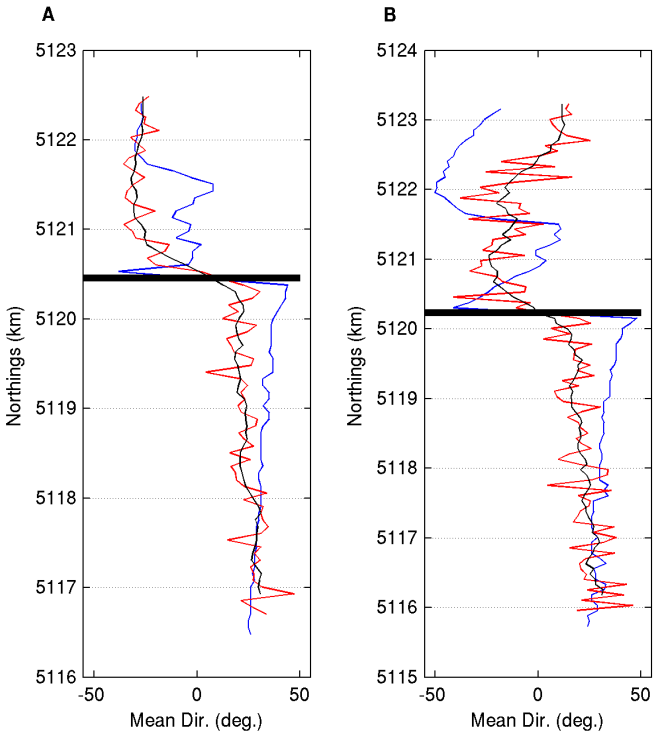

Figure 11: Modeled (blue) and measured (red) mean wave directions for 2 cross-sections located in the radar footprint for March 30 03:00. Offshore mean wave direction is 17^{o} and the velocity in the mouth is -2 m/s. The black line is a 7-point moving average of the measured wave direction. The modeled values are obtained by averaging the direction over the top 4 coherent frequencies obtained from the cross-spectral correlation analysis. Fig. A refers to the west section and Fig. B refers to the east section in Fig. 9.

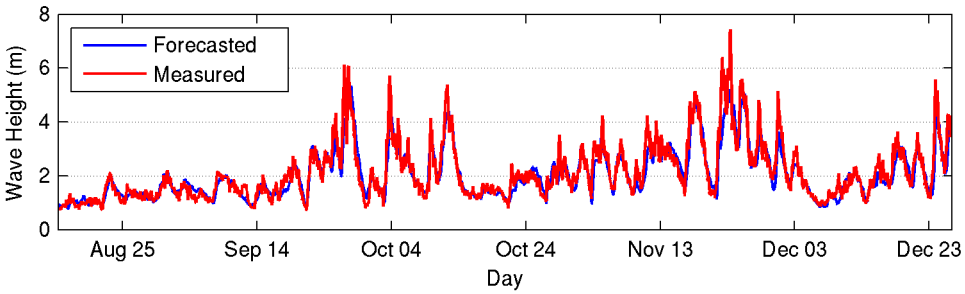

Figure 12: Comparison of wave heights at the CDIP buoy for the 6-month period from August to December, 2011.

Table 3: Forecast results from August to December 2011 at the CDIP buoy. RMSE is the root-mean-squared-error, NRMSE is the normalized root-mean-squared-error.

	H_s offshore	T_p offshore	D_p offshore	H_s buoy	T_p buoy	D_p buoy
RMSE	43 cm	2.8 s	35^o	38 cm	3.1 s	23^o
NRMSE	16%	40%	-	16%	41%	-
BIAS	9.6 m	0.6 s	6^o	-7 cm	0.4 s	-0.4^o
REL. BIAS	4%	5%	-	-3%	4%	-

emphasized by the bathymetric features of the domain. In our case, the propagation in the error from the offshore boundary to the CDIP buoy is very near to linear, with a correlation of 73%. However as the degree of overprediction at the offshore increases, the effect it has on the overprediction at the buoy is reduced, as is seen by the best-fit line in Fig. 13. This deviation from a linear relationship is likely due to refraction effects caused by the variable bathymetry near the CDIP buoy and will be discussed in the next section.

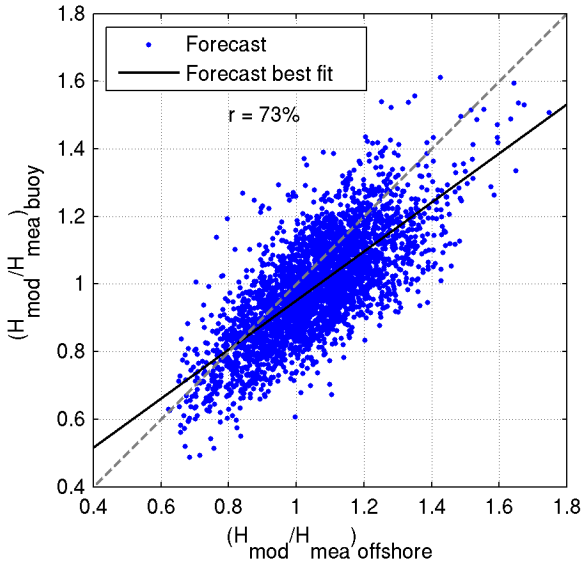

Figure 13: The correlation between the ratio of model to measured wave heights offshore and at the CDIP buoy.

5 Discussion

5.1 Wave transformations due to bathymetry

Wave transformations at the MCR can be generally classified into either bathymetric or current interaction effects. The bathymetry affects the waves on several scales; Astoria canyon, a large bathymetric feature, located 18 km from the entrance to the river in 100 m water depth can significantly alter the large-scale nearshore wave field. As low frequency waves travel over the canyon, they refract over its contours, creating zones of lower and higher wave energy. If waves are coming from the northwest, an area of reduced wave height is seen on Clatsop plains; the area south of the MCR (see Fig. 14). A similar behavior is seen for waves approaching from the southwest, where reduced wave heights occur in the area north of the Columbia River. This effect has been observed in modeling work by García-Medina et al. (2012) and similar behavior in wave refraction have been documented by Long and Özkan-Haller (2005) at the La Jolla and Scripps canyons.

The naturally occurring tidal shoals and outer ebb tidal delta focus energy as waves are diverted to the entrance of the MCR, as is seen by the area of higher wave heights in front of the entrance in Fig. 14. Within the bar, the shoals caused by the disposal mounds create sharp gradients in wave energy, as is seen by the elevated wave heights east and west of the buoy in Fig. 14b.

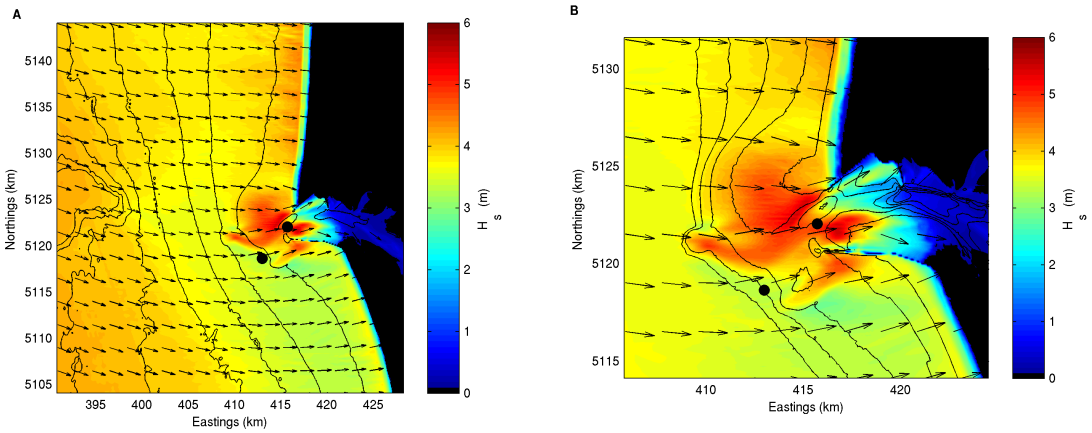

Figure 14: A. Modeled wave heights and mean direction over the model domain for March 5, 21:00. Offshore wave height, peak period and mean direction for this case is 4.3 m, 17 s and -26^{o}, respectively. B. Same as A, but zoomed in to show details near river entrance.

The modeled wave heights at the CDIP buoy are always less than the offshore wave heights. In contrast, the measured wave heights at the buoy shows that this does not occur all of the time since there are some instances where the wave heights at the buoy are larger than the offshore wave heights (see Fig. 15). In the model, regardless of wave direction, waves are diverted from the CDIP buoy to the shoals in front of the entrance, creating a shadow zone at the buoy. In the March hindcast, where the modeled offshore wave heights are measured, when the offshore wave height is approximately 1.2 times or less than the measured buoy wave height, $\left(\left({}^{H_{off}}/_{H_{buoy}}\right)_{mea} \lesssim 1.2\right)$ the model will tend to underpredict the wave height at the buoy. In these situations, the measurements do not indicate strong refraction away from the buoy since the offshore and buoy wave heights are similar, however a shadow zone still occurs in the model, causing the model to underpredict. When the offshore wave height is greater than approximately 1.2 of the measured buoy wave height $\left(\left({}^{H_{off}}/_{H_{buoy}}\right)_{mea} \gtrsim 1.2\right)$, the model will tend to overpredict at the buoy. In this case, the measurements indicate a large shadow zone is occurring near the buoy which is reproduced by the model, but to a lesser extent. The transformation of wave heights from offshore to inshore in the model is limited to an upper bound $\left(\left({}^{H_{off}}/_{H_{buoy}}\right)_{mod} \leq 1.6\right.$ in Fig. 15), but this is not so in the measurements. Looking closer at the case of waves approaching from the northwest, as seen in the right panel of Fig. 14, there is a large focusing of energy at the river mouth and a defocusing of energy at the buoy. In this particular situation, the model over predicts by 40%, which is consistent with Fig. 15, since $\left(\left({}^{H_{off}}/_{H_{buoy}}\right)_{mea} \cong 1.4\right)$. Due to its phase-averaged nature, SWAN has difficulties in reproducing effects that require phase information such as diffraction and wave-wave interactions. In this situation, sharp refraction is occurring over a relatively small spatial scale and the model is unable to resolve this effect correctly.

The forecast follows a similar trend to the hindcast, where the transformation of modeled wave heights from offshore to onshore is limited to a range narrower than the measurements. As stated previously, a large portion of the errors in the forecast are due to the input conditions, but any deviation from the linear correlation seen in Fig. 13 can be explained by the refraction effects at the buoy. When $\left({}^{H_{mod}}/_{H_{mea}}\right)_{off} \gtrsim 0.8$, the model is going to decrease the ratio of modeled to measured wave heights at the buoy, thus leaking energy at this location. This leads to either a further underprediction or a reduction in overprediction in the buoy wave heights compared to the offshore waves heights. This occurs because the model will always create a smaller wave height at the buoy than offshore due to wave defocusing at the buoy.

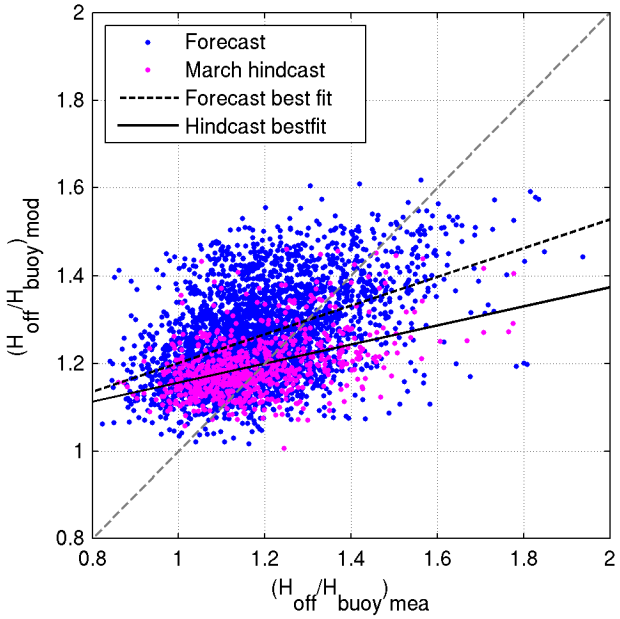

Figure 15: The transformation of wave heights from offshore to the CDIP buoy in the model and the measurements.

When $(H_{mod}/H_{mea})_{off}$ is large, the excess energy present in the model will be diverted to the shoals at the river entrance.

5.2 Wave-current interactions

Within the area of tidal influence, distinct patterns in the wave transformations occur as wave heights increase on ebb tides and decrease on flood tide. Fig. 16 shows the wave heights at the RML obtained from the March hindcast. A clear tidal signature is seen as wave heights increase, at times doubling, during ebb tidal currents and decrease during flood tidal currents. To isolate the effects of the tidal current, the entire March 2010 hindcast is repeated excluding currents. Water surface elevations due to tidal effects are still considered as not doing so would make comparisons ineffective. From Fig. 17, little difference is seen at the CDIP buoy, and changes in wave heights due the currents are mostly insignificant (ΔH $\leq$23 cm), because current velocities at this location are very minor. At the entrance to the mouth (see Fig. 18), the tidal effect is very pronounced, as ebb tidal currents can increase wave heights 20% to 50%. When comparing the wave heights at the CDIP buoy against wave heights at the mouth of the river, it is clear that the currents govern the wave

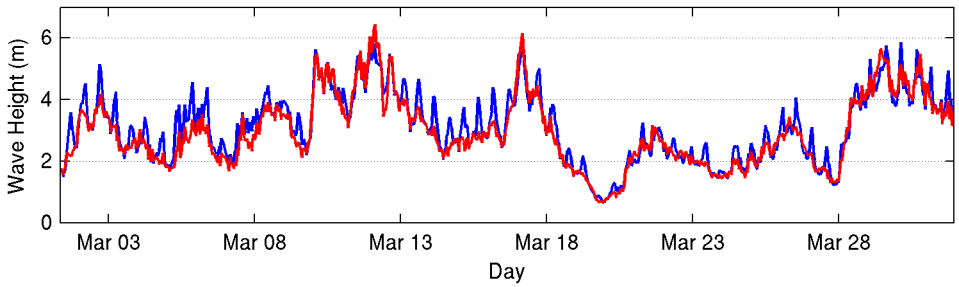

Figure 16: Modeled wave height at the RML (blue) and CDIP buoy (red) during the March 2010 hindcast.

transformations at the river mouth. Within a three hour period, the time between slack and ebb tide, the wave energy at the river mouth can double.

The ebb tidal current has a stronger effect on the wave heights than the flood tidal current, seen by the larger positive changes in Fig. 18; this is primarily because ebb current magnitude is larger than flood current. The maximum ebb and flood currents observed during the hindcast is -1.7 m/s and 0.8 m/s respectively. In addition, the orientation of the tidal plume is such that the typical ebb flow pattern is a jet-like current directed straight offshore, whereas the flood tide is initially more dispersed and eventually converges at the river mouth, and thus strong along-channel velocities are not experienced until further up the river (see Fig. 19b). The effect of these distinct tidal flows is depicted in Fig. 20, where the difference in wave height between current and non-current simulations are shown for a strong ebb tide and strong flood tide case. The difference is defined as $H_{wc} - H_{woc}$, where H_{wc} is runs with currents and H_{woc} is runs without currents. The ebb tide case shows a strong focusing of wave energy in the middle of the channel and another region of wave height increase offshore of the channel. The flood tide case sees a decrease in wave height in the center of the channel. As the wave energy is defocused, it converges on the inside of the jetties, increasing wave heights in this area. The area of tidal effect is only concentrated in between the jetties and unlike the ebb tide case, does not extend offshore.

Over the duration of the hindcast, the pattern of wave height change due to the currents will vary depending on the current strength and direction. But generally, the effect is localized to region in between and in front of the jetties. Fig. 21 and 22 show the maximum and minimum wave height change envelopes. These illustrate the extremes in wave height change due to the presence of the tidal currents. Maximum

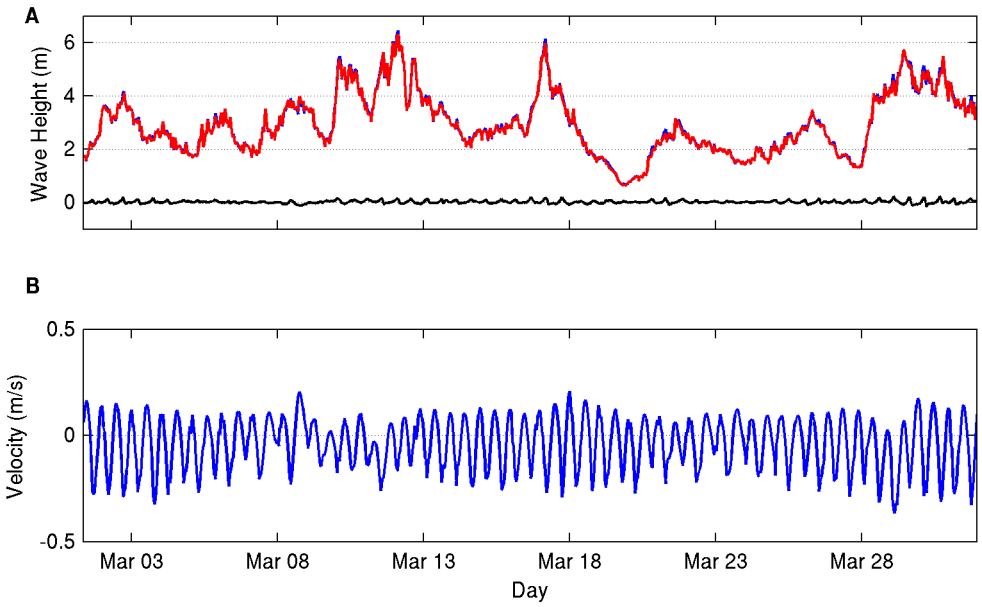

Figure 17: A. Modeled wave heights at the CDIP buoy during March 2010. The blue line includes tidal currents and the red line does not; the black line is the difference between these two simulations. B. along-channel tidal currents at the CDIP buoy.

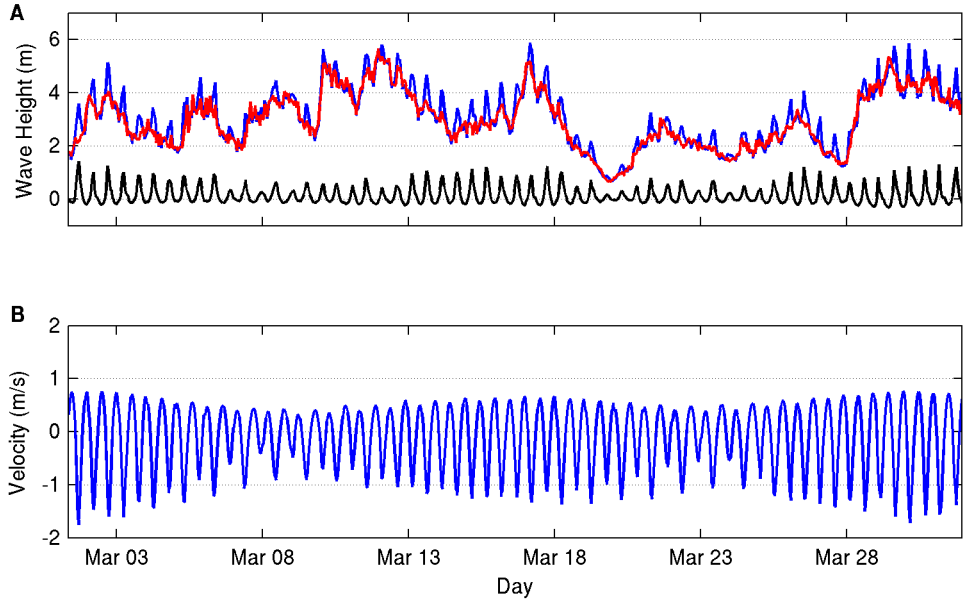

Figure 18: A. Modeled wave heights at the RML during March 2010. The blue line includes tidal currents and the red line does not; the black line is the difference between these two simulations. B. along-channel tidal currents at the RML.

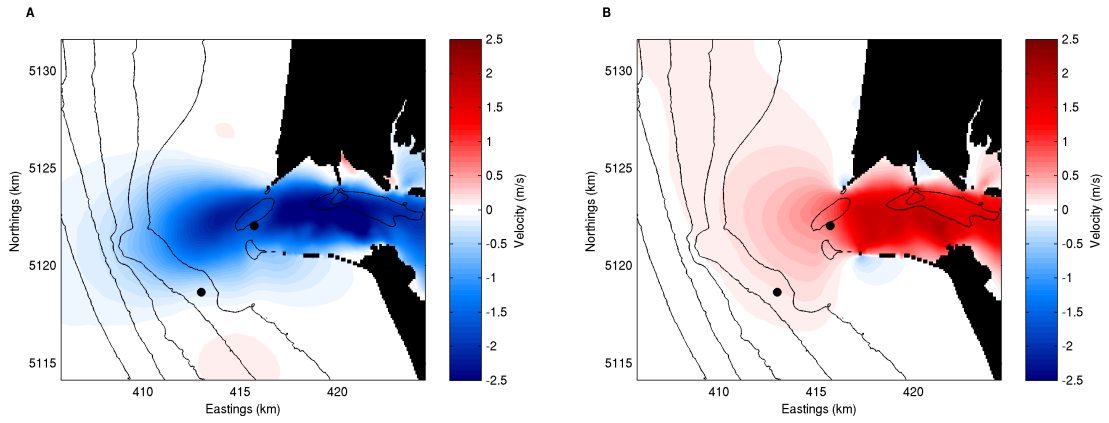

Figure 19: A. along-channel tidal velocity for the strong ebb current case on March 30, 04:00. B. along-channel tidal velocity for the strong flood current case on March 2, 12:00.

change, which is associated with ebb flows (Fig. 21a), shows a peak change of 2.5 m, and is associated with a current of approximately -2 m/s. The effect of the ebb flow is distributed over a narrow plume which extends offshore from the jetties to 40 m water depth. Minimum change, which is generally associated with flood tides, is not as extreme. A maximum decrease of less than 1.5 m is observed and its associated velocity is approximately 1 m/s. The effect of flood tides is concentrated to the location in between the jetties; unlike the ebb tides, it does not extend offshore from the jetties. Interestingly, at some locations, the maximum and minimum change is caused by flood and ebb tides, respectively. For example, in Fig. 22, some locations show a negative velocity. When waves focus due to currents, there will be corresponding areas of defocusing of energy, and this will create locations with a decrease in wave height in the presence of an ebb current. This effect is more prominent on ebb flows since the currents are larger and more concentrated, thus the focusing, and corresponding defocusing of energy is more pronounced.

5.2.1 Effect of tidal plume

The pattern of wave height change due to the currents is highly dependent on the direction of the tidal plume. Due to the orientation of the jetties, the plume will naturally tend to the southwest, but it can be altered by Coriolis and wind effects (Baptista et al., 2005). During ebb flows, this becomes significant since the plume

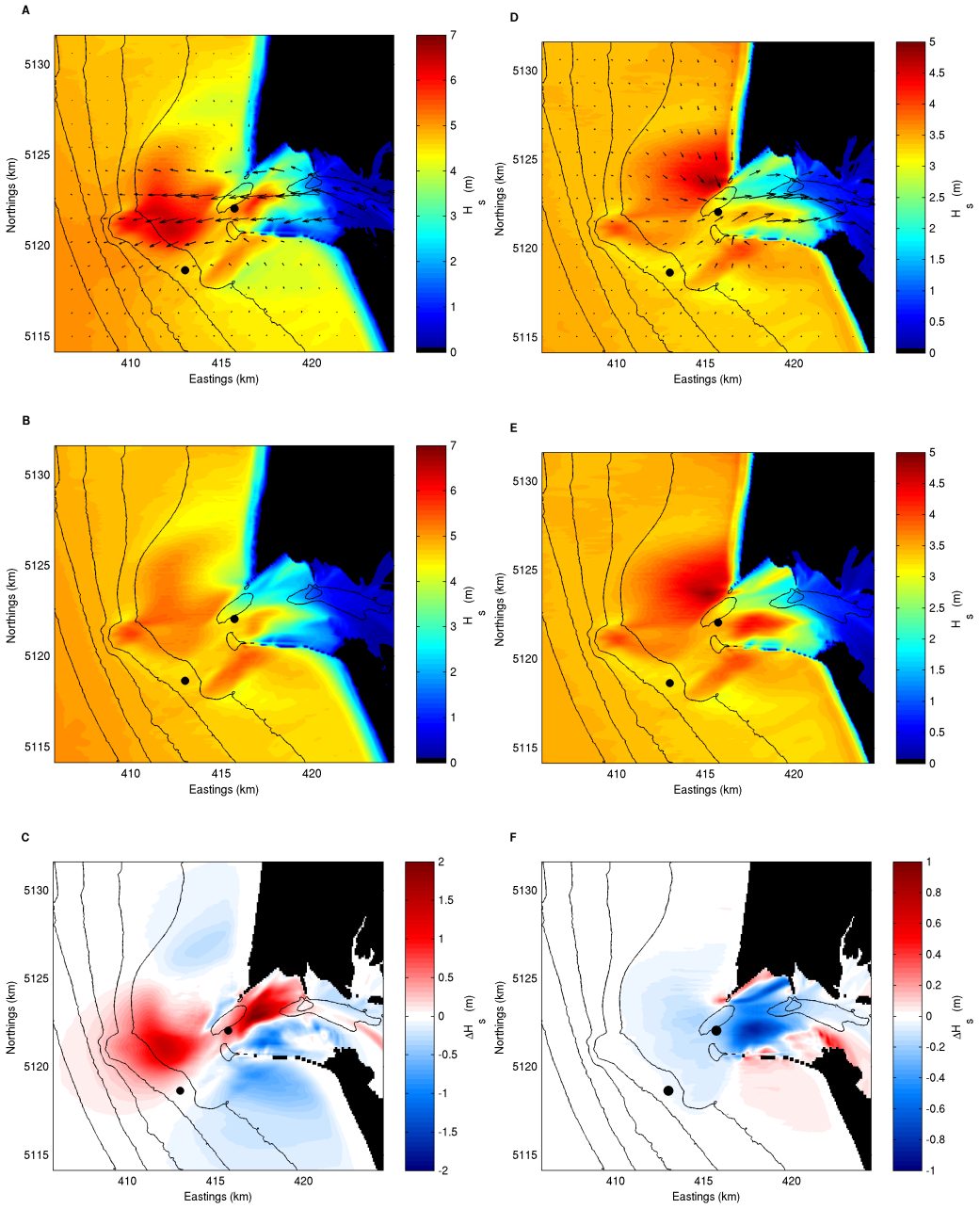

Figure 20: A. Modeled wave height at the MCR on March 30, 04:00, during a particularly large ebb tidal current (see Fig. 19a); offshore wave height, peak period and peak direction is 5.4 m, 13.2 s, and 10^{o}, respectively. B. Modeled wave heights for the same time as Fig. A, but neglecting currents. C. The difference in wave heights between Fig. A and B. D-F. Modeled wave heights at the MCR on March 2, 12:00, during a particularly large flood tidal current (see Fig. 19b); offshore wave height, peak period and peak direction is 3.8 m, 15.5 s and -14^{o}, respectively; with currents (D), without currents (E) and their difference (F).

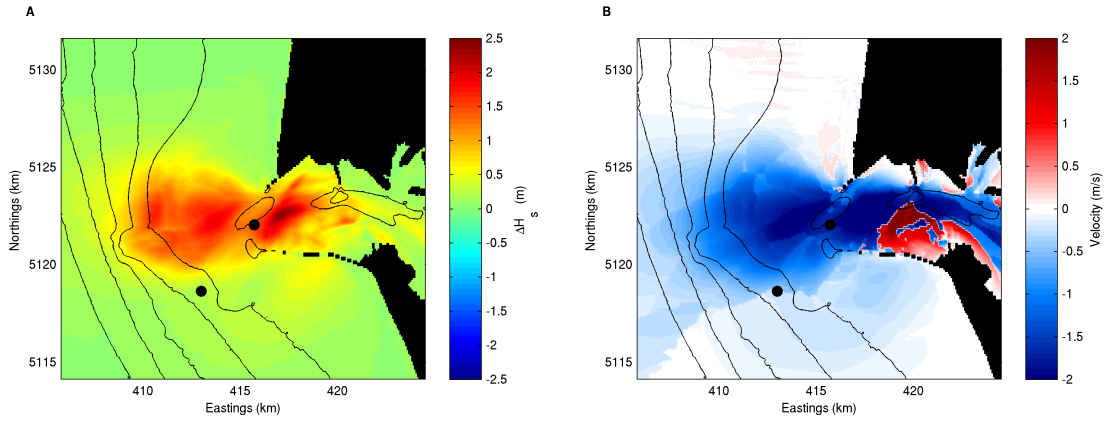

Figure 21: A. Maximum change in wave height due to the currents for every location in the domain over the March 2010 hindcast. B. Wave parallel velocities corresponding to the maximum change in wave height.

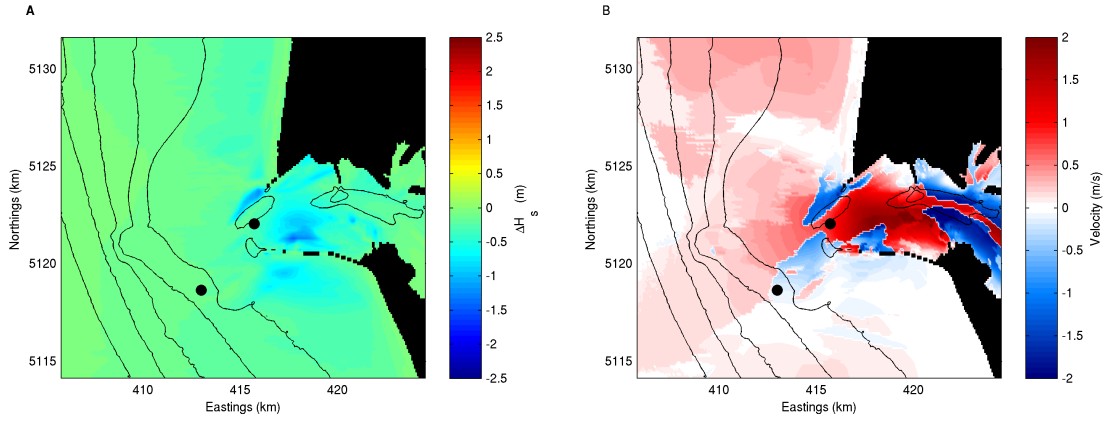

Figure 22: A. Minimum change in wave height due to the currents for every location in the domain over the March 2010 hindcast. B. Wave parallel velocities corresponding to the minimum change in wave height.

orientation governs the direction of the ebb tidal current. The areas of wave height increase due to ebb tides follow the flow pattern of the plume, as is seen in Fig. 23. When the plume is directed northward, areas of wave height increase are seen northwest of the entrance. An area of increased wave height is seen southwest of the channel when the plume is turned to the south.

In both of these examples, regions of decreased wave height are seen north and south of the jetties. These regions, which are caused by the diversion of waves to areas of stronger flow, are also dependent on plume orientation. The decrease south of the channel is more pronounced when the plume is turned southwards and likewise for the lobe north of the channel, when the plume is turned northward. Over multiple tidal cycles, the plume will change direction a number of times, however during the spring, it tends to the southwest direction (Hickey et al., 1998). Fig. 25 shows a larger zone of wave height decrease south of the jetties than north of the jetties, which may indicate that the plume orientation is mostly southward. These regions north and south of the jetty are significant because they experience a tidal signature even though the currents in these locations are weak (see Fig. 24). This makes them interesting locations for instrumentation, since tidal flows are weak but a tidal signature is present in the wave heights. Observations at these locations could give insight into the model's ability to capture current refraction and other wave-current effects.

5.2.2 Effect on direction

The current-induced wave focusing discussed in the previous sections implies that the currents also have an effect on wave direction. The difference in mean direction between current and non-current simulations are determined for the same ebb and flood tide sample cases shown previously (Fig. 26). In both these instances, offshore mean direction is from the southwest. Positive changes in direction indicates waves are being turned more shore parallel and negative changes means waves are being turned more shore normal. In the ebb current case, waves north of the channel are turned toward shore normal, and south of the channel, waves are turned more shore parallel. The resulting wave pattern is oriented towards the region of strongest flow. A similar but opposite effect is seen in the flood case, where the waves are diverted from the area of strongest flow, however the effect is not as substantial because the current, and extent of flow is not as large.

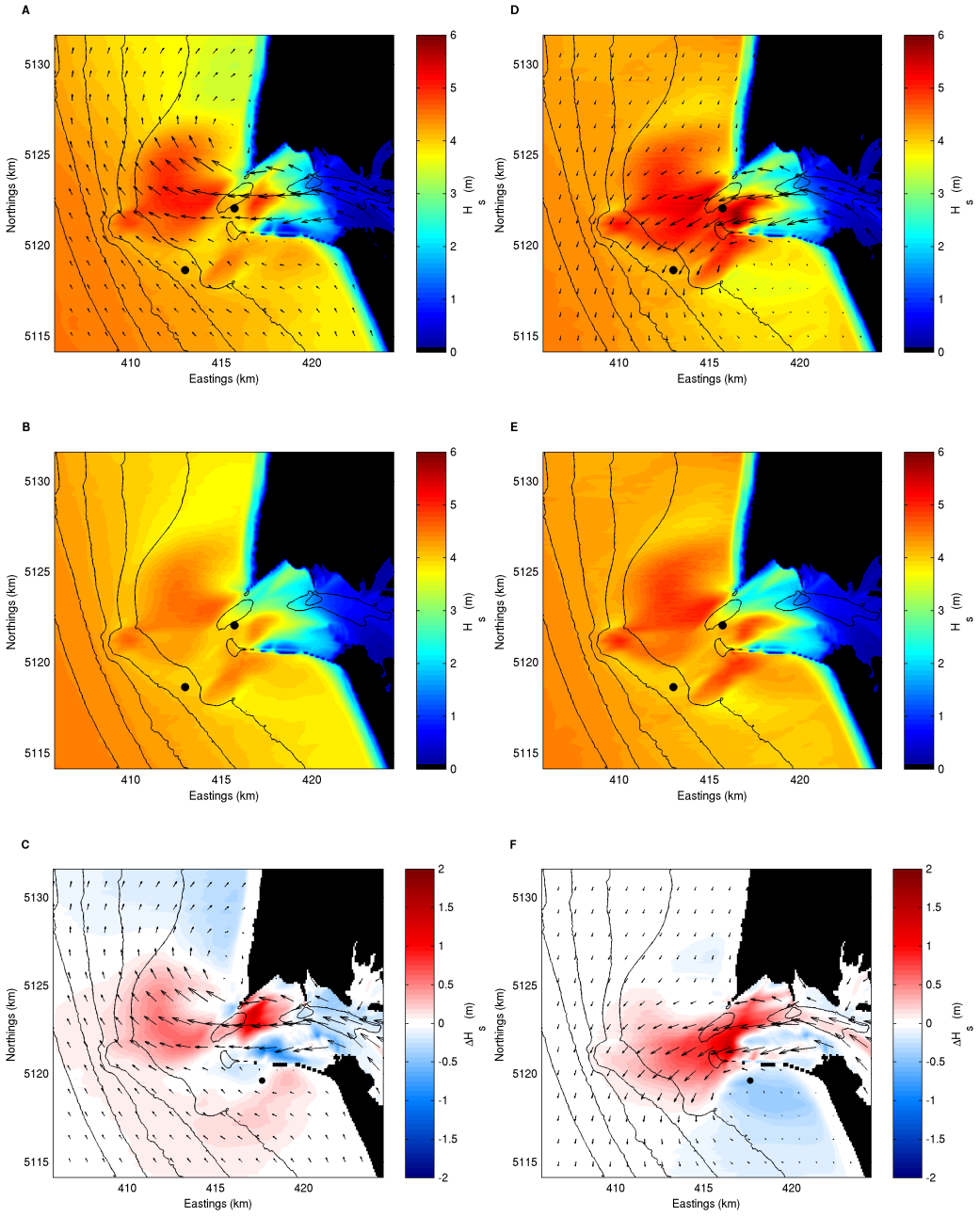

Figure 23: A. Modeled wave heights over the domain for March 29, 04:00, when the plume is oriented to the north; offshore wave height, period and peak wave direction is 4.9 m, 13.2 s and -2º, respectively and the along-channel current in the channel is -1.2 m/s. B. Modeled wave heights for the same time as Fig. A, but neglecting currents. C. The difference in wave heights between Fig. A and B. D-F. Modeled wave heights for March 17, 17:00, when the plume is oriented to the south; offshore wave height, period and peak wave direction is 4.7 m, 13.2 s and -2º, respectively, and the along-channel current in the channel is -1.1 m/s; with currents (D), without currents (E) and their difference (F).

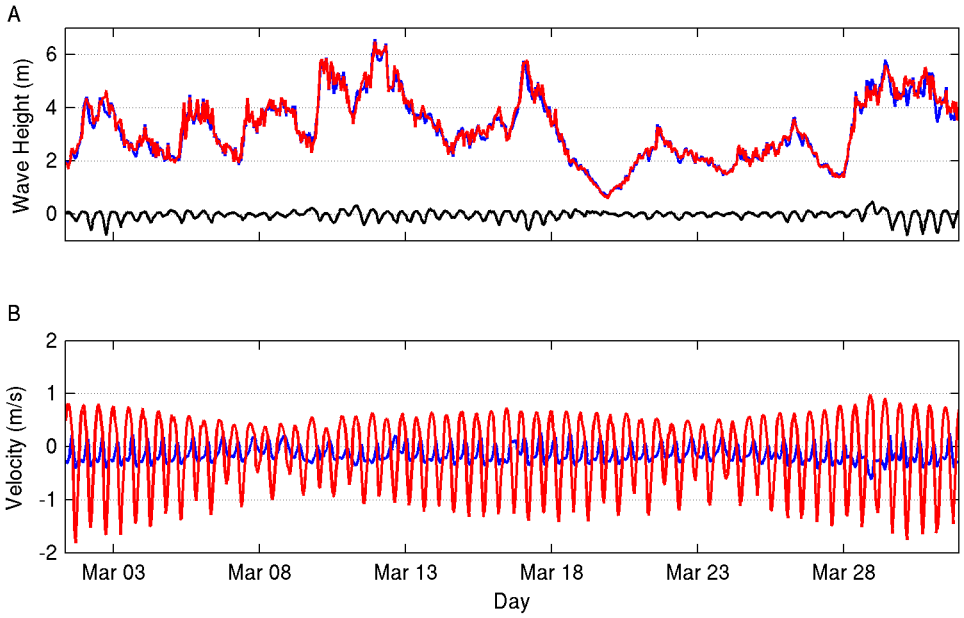

Figure 24: A. Wave heights south the entrance (black point in Fig. 23c and f) with (blue) and without (red) the effect of currents. The black line is the difference between these two simulations. B. Tidal current velocities at that location (blue) and at the RML (red)

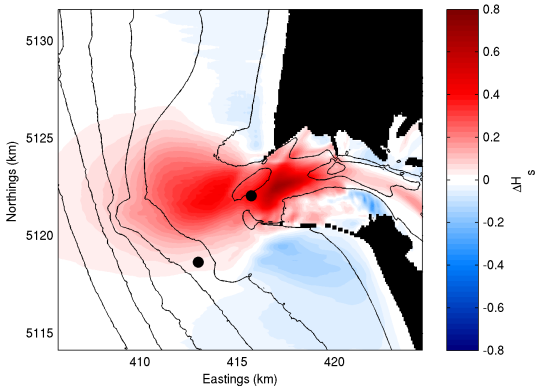

Figure 25: Normalized wave height change due to ebb tidal current, summed over the entire March 2010 hindcast.

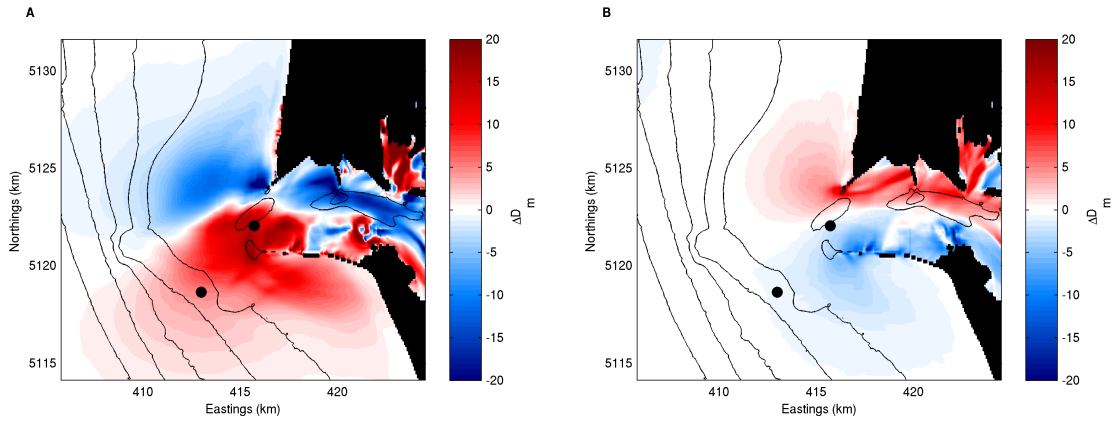

Figure 26: A. Difference in mean wave direction, for March 30, 04:00, between a simulation including and excluding tidal currents for the strong ebb tide case shown in Fig. 19a. B. Difference in mean wave direction, for March 2, 12:00, between a simulation including and excluding tidal currents for the strong flood tide case show in Fig. 19b.

Within the channel and near the south jetty, wave transformation is a mix of current and bathymetric effects. Fig. 27 shows the same cross-sections plotted in Fig. 9, but without the effect of the current. Changes in wave direction occur and the pattern is consistent with what is seen in Fig. 26. However, the evolution in direction across the channel is consistent in both the current and non-current case, thus the behavior of wave refraction observed in the channel is ultimately a function of bathymetry.

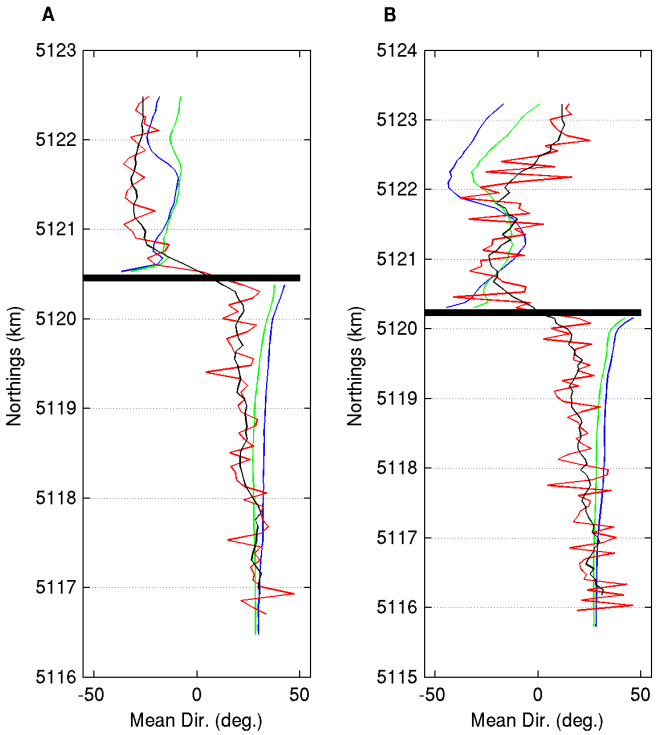

Figure 27: Modeled wave direction with currents (blue) and without currents (green) compared against measured (red) wave directions for 2 cross-sections located in the radar footprint for March 30 03:00. Offshore mean wave direction is 17^{o} and the velocity in the mouth is -2 m/s. The black line is a 7-point moving average of the measured wave direction. The modeled values are obtained by averaging the directions over all frequencies. Fig. A refers to the west section and Fig. B refers to the east section in Fig. 9..

6 Conclusion

The SWAN model was applied to the MCR to determine the governing wave transformation processes at this highly energetic river mouth. The model is validated at 3 locations in the domain with long-term buoy measurements, in-situ measurements and marine radar observations. Best model to data comparison occurs at the CDIP buoy during the March 2010 hindcast, with a NRMSE of 11%. Forecasting waves adds another degree of uncertainty, since errors exist in the initial conditions; despite this, the forecast gave good results at the buoy with a NRMSE of 17%. Comparing the forecast to the March hindcast, it can be said that approximately 45% of the forecast error is derived from the input conditions, since the forecast error is 45% greater than the hindcast error. The remainder of the errors are due to model limitations in the large refraction patterns around the shoals near the buoy. In the channel, the model does not perform as well, but it provides a qualitative representation of the wave-current interaction. Factors such as depth-variable flows and uncertainty in the flow field limit the model performance. In addition, one-way coupling does not capture the effect of the waves on the current, which occur when the waves are breaking due to wave induced currents.

From these hindcasts, some conclusions can be made about the dominant wave transformations at the MCR. Waves near the mouth are heavily influenced by the tidal current and plume direction. On ebb tide, the area of tidal influence is confined to a plume-like structure, extending approximately 10 km offshore from the jetties, depending on current magnitude. On flood tides, the tidal current effect on the waves is less pronounced and significant wave height change occurs primarily in between the jetties and in the channel. Outside of the region of tidal influence, waves are heavily affected by the bathymetry; shoals located in front of the entrance focus waves to the river mouth.

The forecast is fully operational, giving wave information throughout the domain 45 hours in advance. The results of the forecast are currently shared with the Columbia River Bar Pilots, who are responsible for the navigation of large vessels throughout the river way, and thus have a vested interested in the short-term prediction of wave heights. Even though this forecast is at an experimental stage, the information it provides is still valuable since it includes the effect of the currents, which is something the bar pilots have not had access to up until this point.

Bibliography

Allan, J. C., Komar, P. D., 2002. Extreme storms on the Pacific Northwest coast during the 1997-98 el niño and 1998-99 la niña. Journal of Coastal Research 18 (1), 175–193.

Baptista, A. M., Zhang, Y., Chawla, A., Zulauf, M., Seaton, C., Myers III, E. P., Kindle, J., Wilkin, M., Burla, M., Turner, P. J., 2005. A cross-scale model for 3D baroclinic circulation in estuary-plume-shelf systems: II. Application to the Columbia River. Continental Shelf Research 25 (7–8), 935–972.

Battjes, J. A., Janssen, J. P. F. M., 1978. Energy loss and set-up due to breaking of random waves. In: 16th International Conference on Coastal Engineering. ASCE, pp. 569–587.

Booij, N., Ris, R. C., Holthuijsen, L. H., 1999. A third-generation wave model for coastal regions 1. Model description and validation. Journal of Geophysical Research 104 (C4), 7649–7666.

Elias, E., Gelfenbaum, G., 2009. Modeling processes controlling sediment transport at the mouth of the Columbia River. In: Coastal Dynamics 2009.

Elias, E., Gelfenbaum, G., van der Westhuysen, A., 2012. Validation of a coupled wave-flow model in a high-energy setting: The Mouth of the Columbia River. Journal of Geophysical Research 117.

García-Medina, G., Özkan-Haller, H., Ruggiero, P., Oskamp, J., 2012. A nearshore wave forecasting system for the US Pacific Northwest. Weather and Forecasting (in review).

González, F. I., 1984. A case study of wave-current-bathymetry interactions at the Columbia River entrance. Journal of Physical Oceanography 14 (6), 1065–1078.

González, F. I., Cokelet, E. D., Gower, J. F. R., Mulhern, M. R., 1985. SLAR and in-situ observations of wave-current interaction on the Columbia River Bar. In: The Ocean Surface. D. Reidel, New York, pp. 303–310.

Gorrell, L., Raubenheimer, B., Elgar, S., Guza, R. T., 2011. SWAN predictions of waves observed in shallow water onshore of complex bathymetry. Coastal Engineering 58, 510–516.

Haglund, M. E., 2011. World's most dangerous: a history of the Columbia River Bar, its pilots and their equipment. Columbia River Maritime Museum, Astoria, Oregon.

Hamilton, P., 1990. Modelling salinity and circulation for the Columbia River Estuary. Progress in Oceanography 25 (1–4), 113–156.

Hickey, B. M., Pietrafesa, L. J., Jay, D. A., Boicourt, W. C., 1998. The Columbia River plume study: Subtidal variability in the velocity and salinity fields. Journal of Geophysical Research 103 (C5), 10,339–10,368.

Horner-Devine, A. R., 2009. The bulge circulation in the Columbia River plume. Continental Shelf Research 29 (1), 234–251.

Jonsson, I. G., 1990. Wave-current interactions. In: The Sea. Vol. 9A. Wiley-Interscience, Hoboken, N.J., pp. 65–120.

Kaminsky, G. M., Ruggiero, P., Buijsman, M. C., McCandless, D., Gelfenbaum, G., 2010. Historical evolution of the Columbia River littoral cell. Marine Geology 273 (1–4), 96–126.

Kirby, J. T., Chen, T. M., 1989. Surface waves on vertically sheared flows: Approximate dispersion relations. Journal of geophysical research 94 (C1), 1013–1027.

Komen, G. J., Hasselmann, S., Hasselmann, K., 1984. On the existence of a fully developed wind-sea spectrum. Journal of Physical Oceanography 14, 1271–1285.

Long, J. W., Özkan-Haller, H. T., 2005. Offshore controls on nearshore rip currents. Journal of geophysical research 110 (C12007), 21 p.

Michalsen, D. R., Moritz, H. R., McKillip, D. J., 2006. Potential physical impacts of a littoral drift restoration project - Mouth of the Columbia R., USA. In: Proceedings of the 30t̂h International Conference on Coastal Engineering. Vol. 2. pp. 1964–1976.

Moghimi, S., Gayer, G., Günther, H., Shafieefar, M., 2005. Application of third generation shallow water wave models in a tidal environment. Ocean Dynamics 55 (1), 10–27.

Moritz, H. R., Gelfenbaum, G. R., Kaminsky, G. M., Ruggiero, P., Oltman-Shay, J., Mckillip, D. J., 2007. Implementing regional sediment management to sustain navigation at an energetic tidal inlet. In: Coastal Sediments 2007. ASCE.

Moritz, H. R., Gelfenbaum, G. R., Ruggiero, P., 2005. Morphological implications of oceanographic measurements acquired along a mega-transect at the mouth of the Columbia River, USA. In: AGU Fall Meeting. Abstract OS23A-1534.

Mortiz, H. R., Moritz, H. P., Hays, J. R., Sumerell, H. R., 2003. 100-Years of shoal evolution at the mouth of the Columbia River: Impacts on channel, structures, and shorelines. In: Coastal Sediment '03, East meets West productions.

Olabarrieta, M., Warner, J. C., Kumar, N., 2011. Wave-current interaction in Willapa Bay. Journal of Geophysical Research 116, 27 p.

Peregrine, D. H., 1976. Interaction of water-waves and currents. Advances in Applied Mechanics 16, 9–117.

Plant, N. G., Holland, T. K., Haller, M. C., 2008. Ocean wavenumber estimations from wave-resolving time series imagery. IEEE Transactions on Geoscience and Remote Sensing 46 (9), 2644–2658.

Ris, R. C., Holthuijsen, L. H., 1996. Spectral modelling of current induced wave-blocking. In: Proceedings of the 25ˆth International Conference on Coastal Engineering. Vol. 1. ASCE, pp. 1247–1254.

Rogers, W. E., Hwang, P. A., Wang, D. W., 2003. Investigation of wave growth and decay in the SWAN model: Three Regional-Scale applications. Journal of Physical Oceanography 33 (2), 366–389.

Rogers, W. E., Kaihatu, J. M., Hsu, L., Jensen, R. E., Dykes, J. D., Holland, K. T., 2007. Forecasting and hindcasting waves with the SWAN model in the Southern California Bight. Coastal Engineering 54 (1), 1–15.

Ruggiero, P., Kaminsky, G. M., Gelfenbaum, G., Voigt, B., 2005. Seasonal to interannual morphodynamics along a high-energy dissipative littoral cell. Journal of Coastal Research 21 (3), 553–578.

Simenstad, C. A., Small, L. F., McIntire, C. D., Jay, D. A., Sherwood, C., 1990. Columbia River Estuary studies: An introduction to the estuary, a breif history, and prior studies. Progress in Oceanography 25 (1–4), 1–13.

Tillotson, K., Komar, P. D., 1997. The wave climate of the Pacific Northwest (Oregon and Washington): A comparison of data sources. Journal of Coastal Research 13 (2), 440–452.

USACE, 2003. Mouth of the Columbia River shallow water ocean dredged material disposal site: Supplemental evaluation of optimized site utilization and assessment of potential wave-related impacts. Tech. rep., USACE, Portland District.

USACE, 2008. 2008 annual use plan: Management of open water dredged material disposal sites: Mouth of the Columbia River, OR and WA. Tech. rep., USACE, Portland District.

van der Westhuysen, A., Elias, E., 2010. Validation of wave-current interaction modelling in the Western Scheldt and the Columbia River Mouth. Tech. Rep. 1202120-004, Deltares.

van der Westhuysen, A. J., Zijlema, M., Battjes, J. A., 2007. Nonlinear saturation-based whitecapping dissipation in SWAN for deep and shallow water. Coastal Engineering 54 (2), 151–170.

Zhang, Y., Baptista, A. M., Myers III, E. P., 2004. A cross-scale model for 3D baroclinic circulation in estuary-plume-shelf systems: I. Formulation and skill assessment. Continental Shelf Research 24 (18), 2187–2214.